

PAPER • OPEN ACCESS

Evidence for phase transitions in $CoFe_2O_4$ and NiCo₂O₄ thin films in temperature-dependent Xray photoelectron spectroscopy

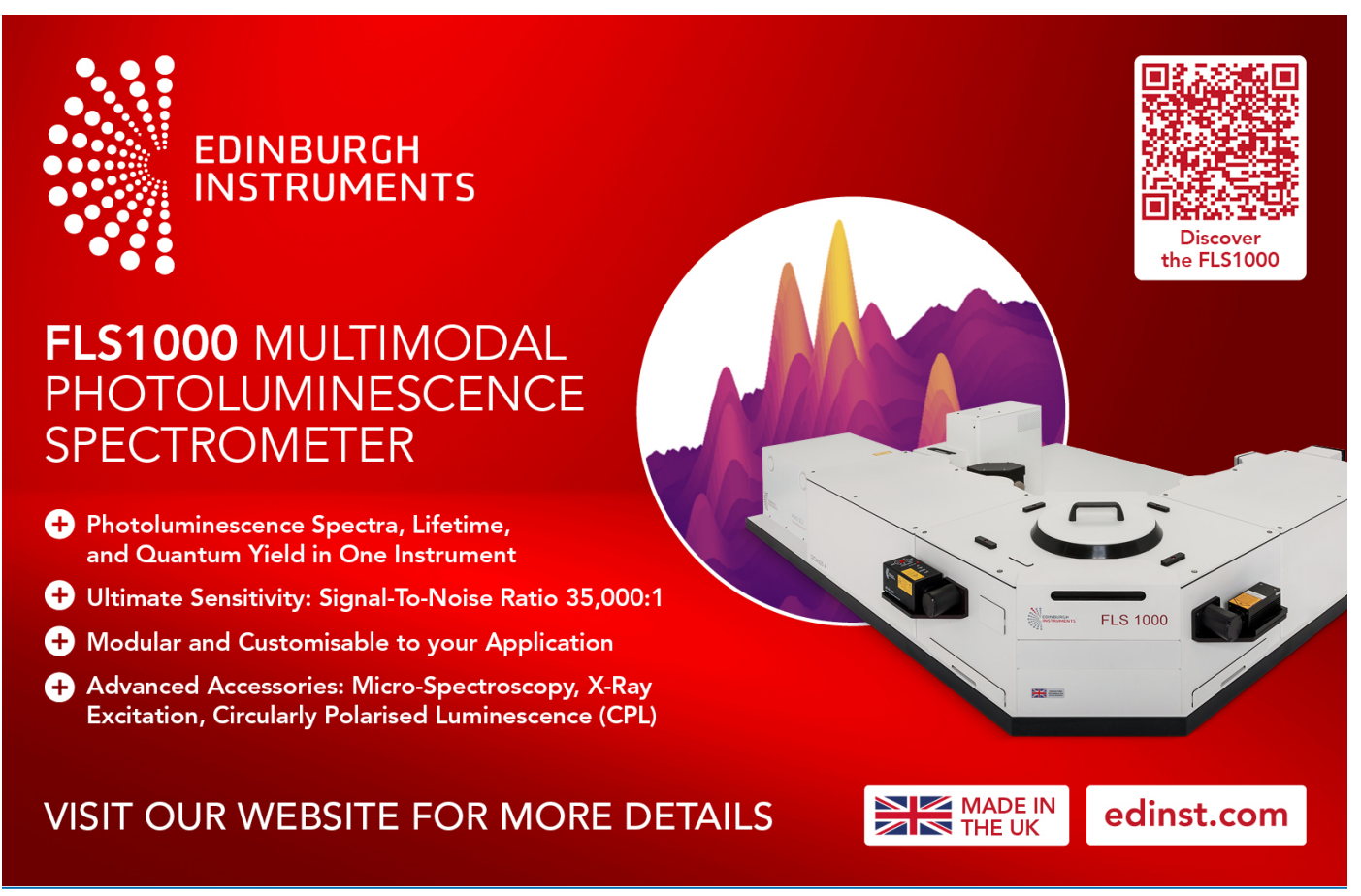
To cite this article: Arjun Subedi et al 2024 J. Phys. D: Appl. Phys. 57 495301

View the article online for updates and enhancements.

You may also like

- P(AN-co-MMA) nanofiber membrane decorated with greenly synthesized nanoparticles for heavy metal removal: a competitive study Abeer Syed, Enshirah Da'na, Amel Taha
- Challenging Issues for Terabit-Level Perpendicular STT-MRAM Jea-Gun Park
- An interpretation for the components of 2p_{3/2} core level x-ray photoelectron spectra of the cations in some inverse

Arjun Subedi, Detian Yang, Wai Kiat Chin et al.



J. Phys. D: Appl. Phys. 57 (2024) 495301 (14pp)

https://doi.org/10.1088/1361-6463/ad5aa8

Evidence for phase transitions in CoFe₂O₄ and NiCo₂O₄ thin films in temperature-dependent X-ray photoelectron spectroscopy

Arjun Subedi*, Detian Yang, Xiaoshan Xu and Peter A Dowben

Department of Physics and Astronomy, Jorgensen Hall, University of Nebraska, Lincoln, NE 68588, United States of America

E-mail: arjun.subedi@huskers.unl.edu

Received 17 February 2024, revised 11 May 2024 Accepted for publication 21 June 2024 Published 23 September 2024



Abstract

X-ray photoelectron spectroscopy (XPS) shows that dramatic changes in the core level binding energies can provide strong indications of transitions between more dielectric and more metallic CoFe₂O₄ and NiCo₂O₄ thin films. These significant variations in the XPS core level binding energies are possible with a combination of annealing and oxygen exposure; however, the behaviors of the $CoFe_2O_4$ and $NiCo_2O_4$ thin films are very different. The XPS Co and Fe $2p_{3/2}$ core levels for the CoFe₂O₄ thin film at room temperature show large photovoltaic surface charging, leading to binding energy shifts, characteristic of a highly dielectric (or insulating) surface at room temperature. The photovoltaic charging, observed in the XPS binding energies of the Co and Fe $2p_{3/2}$ core levels, decreases with increasing temperature. The XPS core level binding energies of CoFe₂O₄ thin film saturated at lower apparent binding energies above 455 K. This result shows that the prepared CoFe₂O₄ thin film can be dielectric at room temperature but become more metallic at elevated temperatures. The dielectric nature of the CoFe₂O₄ thin film was restored only when the film was annealed in sufficient oxygen, indicating that oxygen vacancies play an important role in the transition of the film from dielectric (or insulating) to metallic. In contrast, the XPS studies of initially metallic NiCo₂O₄ thin film demonstrated that annealing NiCo₂O₄ thin film led to a more dielectric or insulating film. The original more metallic character of the NiCo₂O₄ film was restored when the NiCo₂O₄ was annealed in sufficient oxygen. Effective activation energies are estimated for the carriers from a modified Arrhenius-type model applied to the core level binding energy changes of the CoFe₂O₄ and NiCo₂O₄ thin films, as a function of temperature. The origin of the carriers, however, is not uniquely identified. This work illustrates routes to regulate the surface metal-to-insulator transition of dielectric oxides, especially in the case of insulating NiCo₂O₄ thin film that can undergo reversible metal-to-insulator transition with temperature.

Supplementary material for this article is available online

Keywords: electronic phase transition, inverse spinel oxides, x-ray photoelectron spectroscopy

© BY

Original content from this work may be used under the terms of the Creative Commons Attribution 4.0 licence. Any fur-

ther distribution of this work must maintain attribution to the author(s) and the title of the work, journal citation and DOI.

^{*} Author to whom any correspondence should be addressed.

1. Introduction

The oxide at the surface of CoFe₂O₄ (CFO) thin films has been identified to be different from the bulk [1]. The surface weighted component was distinguished from the bulk weighted component for the Co and Fe $2p_{3/2}$ core levels in angle-resolved x-ray photoelectron spectroscopy (ARXPS) of CFO thin films. In that study, binding energy corrections were necessary to consider the photovoltaic charging in the XPS core level binding energies, indicating that CFO thin films were dielectric. Such binding energy shifts in the XPS of insulating samples are common due to the uncompensated buildup of surface charges. When the photoelectron current leaving the sample is not sufficiently compensated, due to the lack of conductance through an insulating or non-metallic sample, the result is a positive potential developed at the surface [2–4] and makes the sample's surface an electron-deficient region. This potential (V) developed, at the surface of an insulator with a dielectric constant (ϵ) , is related to the volume charge density build-up (ρ) by the Poisson's equation:

$$\frac{d^2V}{dz^2} = -\frac{\rho}{\epsilon} \tag{1}$$

where V is a function along the z direction normal to the surface such that, for a thin dielectric film of a certain thickness (t), expression (1), for the grounded sample holder and analyzer, yields [5, 6]:

$$V \sim \frac{\sigma t}{\epsilon}$$
 (2)

where σ is the surface charge density build-up. For a conductor, the dielectric constant (ϵ) is ideally infinite. From equation (2), there is no potential build-up at the surface for the conductor. In contrast, for an insulator, finite value of the dielectric constant (ϵ) creates a finite potential. The development of such potential at the surface of an insulating sample in XPS is called photovoltaic surface charging and is a well-established concept [5–8]. The positive potential at the surface reduces photoelectron's kinetic energy during the photoemission process; hence, it leads to an increase in the apparent binding energy, as the surface charging shifts the core level binding energies in photoemission.

For CFO thin films, questions regarding the temperature dependence of the surface photovoltaic charging and the possible role of oxygen vacancies at the surface remain unresolved. The effects of oxygen defects or vacancies can be crucial because the loss of oxygen from the surface, when an oxide sample is annealed at higher temperature, can cause drastic changes in the electronic properties of the oxide materials [9–11]. For instance, oxygen vacancies can contribute to the conductivity [12, 13], change in crystal color [11, 14], make occupied states appear in the band gap [15], drive phase transitions [16–18], play important roles in resistive switching [19, 20] and photocatalytic effects [21, 22], affect

the behavior of electrocatalysts [23], and participate in the electrochemical redox and structure-work function-activity relationship in some oxides [24, 25]. Here, we explore the role of oxygen vacancies on the temperature-dependent changes in the surface charging of CoFe₂O₄ (CFO) and NiCo₂O₄ (NCO) thin films. Both CFO and NCO are inverse spinel ferrimagnetic oxides. Although CFO thin films tend to be insulating, NCO thin films, despite being structurally similar to CFO, can be conducting [26–29].

2. Experimental details

(111)-oriented epitaxial CoFe₂O₄ (5 nm) and NiCo₂O₄ (10 nm) thin films were grown on -Al₂O₃ (0001) substrates by pulsed laser deposition with an oxygen pressure of 5 mTorr at 530°C and 300°C, respectively [26]. The KrF excimer laser, with a wavelength of 248 nm, was employed to ablate the CFO and NCO targets with a pulse energy of 120 mJ and a repetition rate of 4 Hz. The growth processes were *in situ* monitored by a reflection high energy electron diffraction (RHEED) system. XPS spectra were acquired using an un-monochromatized SPECS X-ray Mg K $_{\alpha}$ anode (hv=1253.6~eV) source (3 cm from the sample) and VG100AX hemispherical analyzer at different temperatures.

The ARXPS technique has been applied to the investigation of the surface composition of other oxides [30-32] and is a common approach for determining the surface composition of multicomponent oxides. Here, ARXPS measurements were performed at six different emission angles. The emission angle is, here, defined as the photoelectron takeoff angle with respect to the sample surface normal (figure S1 of the supplementary information (SI)). In cases where photovoltaic charging needed to be eliminated so as to ascertain the correct core level XPS binding energies, the ARXPS spectra were corrected using the adventitious carbon 1s (AdC 1s) binding energy position, for each of the angles. In the ARXPS technique, the measurements at higher photoelectron emission angles (more grazing to the surface) are more surface sensitive than the measurements at lower angles, as described elsewhere [1, 33, 34]. In this study, the acceptance angle of the hemispherical analyzer for the ARXPS measurements is $\pm 10^{\circ}$, and the possible error in the binding energy measurements is ± 0.2 eV.

For the samples studied here, no compelling signatures of photoelectron diffraction were observed in the angle-resolved XPS measurements. For the temperature-dependent XPS measurements, the temperature was measured with a type-K thermocouple. The XPS data were acquired after a steady temperature was reached, for each value of temperature. The temperature fluctuations of ± 1 K does occur during the XPS measurements. Low energy electron diffraction of NCO does indicate a six-fold diffraction pattern of the (111) surface, indicating that there is surface order (figure 1), but the diffraction spots are diffused and the background is high, indicative of a high density of surface defects.

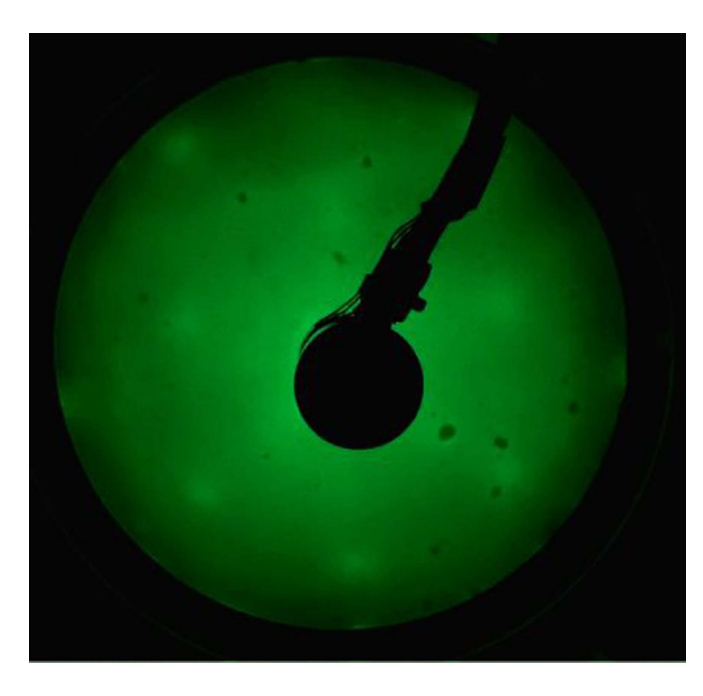


Figure 1. The low energy electron diffraction (LEED), obtained at an electron kinetic energy of 203 eV and screen voltage of 5 kV of 10 nm thick $NiCo_2O_4(111)$ film grown on single-crystal $Al_2O_3(0001)$.

3. Results and discussion

3.1. Spectroscopic evidence that the surface is distinct from the bulk

The angle-resolved $2p_{3/2}$ core level XPS from epitaxial CFO and NCO reaffirms the contention that the surface is different from the bulk not only for CFO but also for NCO thin films. For Ni, Fe, and Co, in the inverse spinel oxides, the $2p_{3/2}$ core level XPS spectra are all characterized by two overlapping components below the $2p_{3/2}$ core level envelope and a satellite feature (S) (as noted elsewhere [1, 26, 29, 33, 35–53] and the references therein). Although the satellite XPS feature is common to transition metal oxides, for CFO and NCO, the $2p_{3/2}$ core level satellite feature is viewed to be the strongest for Co in CFO and the strongest for Ni in NCO while comparing the transition metal 2p spectra, as seen in figures 2 and 3.

3.1.1. $CoFe_2O_4(111)$. Some representative ARXPS spectra, for CFO at room temperature, are depicted in figure 2. The Co $2p_{3/2}$ core level spectra were fitted for three components: P_1 at 779.4 eV, P_2 at 781.4 eV, and S (satellite) at 785.9 eV binding energies. The binding energy of the main Co $2p_{3/2}$ core level peak at normal emission (0°) is found to be at 779.7 eV, which is in excellent agreement with the 779.9 \pm 0.2 eV reported elsewhere [35]. The Fe $2p_{3/2}$ core level spectra were fitted for two component peaks: P_1 at binding energies of 709.6 eV and P_2 at 711.6 eV. The binding energy of the main Fe $2p_{3/2}$ core level peak at normal emission is found to be at 710.3 eV, which is in good agreement with the value of 710.6 \pm 0.2 eV reported elsewhere [36]. The P_1/P_2 ratio for the Co $2p_{3/2}$ core

level components decreases with increasing emission angle, whereas the P_1/P_2 ratio for the Fe $2p_{3/2}$ core level components increases, as seen in figure 2. This result means that P_1 (P₂) is a surface (bulk) weighted component of the Fe $2p_{3/2}$ core level, and P_2 (P₁) is a surface (bulk) weighted component for the Co $2p_{3/2}$ core level. The binding energy difference of 2 eV between the components P_1 and P_2 is therefore an apparent surface-to-bulk core level shifts in the binding energies of Co and Fe core levels, as described elsewhere [1, 33].

The CFO thin film surface was found to be rich in cobalt, as indicated by the calculated surface stoichiometry of Co_{2.1}Fe_{1.0}O_{3.9} derived from XPS. Such cobalt-rich surfaces for CFO thin films were also indicated by prior studies of several CFO thin films [1, 33]. Thus, the CFO surface differs from the bulk not only because coordination at the surface is reduced from the bulk but also because the surface stoichiometry differs from the bulk. The different surface stoichiometries and the facility for surface oxygen vacancy formation, as discussed below, may result in a surface oxide that differs from the bulk, and thus contribute to the observed surface-to-bulk core level shifts discussed above.

3.1.2. NiCo₂O₄(111). To provide a comparison between CFO and NCO thin film surfaces, we conducted angleresolved XPS measurements on two different NCO thin films, which were prepared at different oxygen pressures: one NCO thin film was prepared at the oxygen pressure of 5 mTorr and the other was prepared at the higher oxygen pressure of 30 mTorr. Figure 3 shows the XPS Ni and Co $2p_{3/2}$ core level spectra of NCO at room temperature. The Ni $2p_{3/2}$ core level spectra for the 10 nm thick NCO prepared at a lower oxygen pressure of 5 mTorr, as shown in figure 3(a), contain three components: P₁ at 853.7 eV, P₂ at 855.5 eV, and a satellite feature (S) at 860.7 eV. At normal emission (0°), the main (overall) peak position of the Ni $2p_{3/2}$ core level was found to be at the binding energy of 854.3 eV, which is slightly higher than previously reported values [37, 38]. For the sample prepared at 5 mTorr oxygen pressure, the Co $2p_{3/2}$ core level also contains three components: P_1 at 779.0 eV, P_2 at 780.8 eV, and S (satellite) at 785.2 eV, as shown in figure 3(b). The main peak position of the Co $2p_{3/2}$ core level at normal emission was found to be at the binding energy of 779.3 eV, which is slightly smaller than the values reported elsewhere [37, 38]. For NCO film prepared at the higher oxygen pressure of 30 mTorr, the resulting Ni and Co $2p_{3/2}$ core level spectra show that the main core level peaks are shifted by 0.7 eV to higher binding energies, indicating a more oxidized surface, as shown in figures 3(c) and (d). Both the 10 nm thick NiCo₂O₄ thin films prepared at 5 mTorr and 30 mTorr exhibit surface nickel enrichment, as indicated by the ratio of Ni to Co $2p_{3/2}$ core level XPS intensities normalized by analyzer transmission and photoemission cross-section. The stoichiometries, at the surface, for the 10 nm thick NCO thin films prepared at oxygen pressure of 5 mTorr and 30 mTorr are Ni_{1.7}Co_{2.1}O_{3.2} and Ni_{1.3}Co_{1.8}O_{3.8}, respectively.

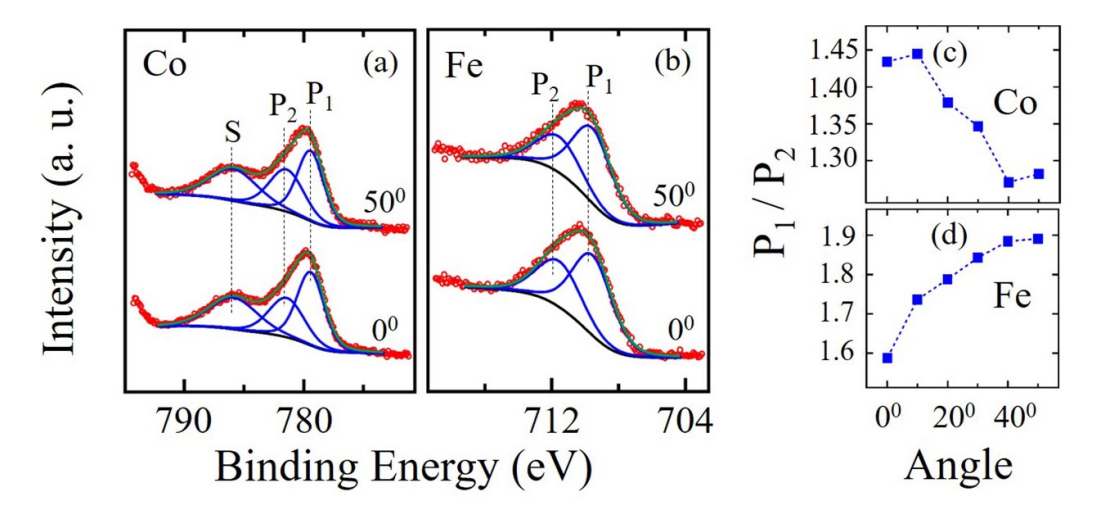


Figure 2. The angle-resolved x-ray photoelectron spectroscopy of 5 nm thick $CoFe_2O_4(111)$ (CFO) thin film. Representative XPS core level spectra of the (a) $Co 2p_{3/2}$ and (b) Fe $2p_{3/2}$ core levels, at emission angles of 0° and 50° with respect to the surface normal, are shown. The ratios between the XPS core level components (P_1/P_2) are plotted as a function of the photoelectron emission angle for (c) Co and (d) Fe core levels. In the panels (a) and (b), red circles, green solid lines, blue solid lines, and black solid lines are raw data, fitted lines, component peaks, and background levels, respectively.

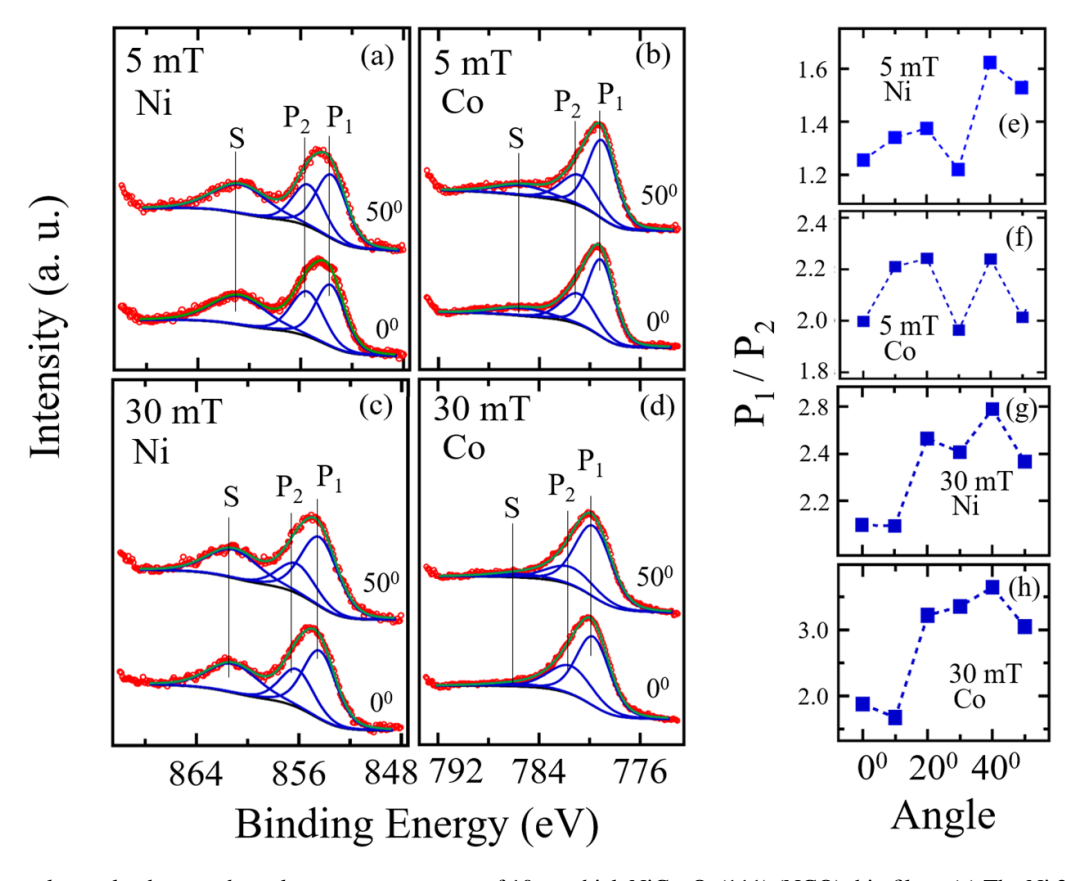


Figure 3. The angle-resolved x-ray photoelectron spectroscopy of 10 nm thick $NiCo_2O_4(111)$ (NCO) thin films. (a) The Ni $2p_{3/2}$ and (b) the Co $2p_{3/2}$ XPS core level spectra taken at emission angles of 0° and 50° with respect to the surface normal of the sample grown at 5 mTorr (mT) pressure. (c) The Ni $2p_{3/2}$ and (d) the Co $2p_{3/2}$ XPS core level spectra at 0° and 50° emission angles with respect to the surface normal of the sample grown at 30 mTorr (mT) pressure. The ratios between the $2p_{3/2}$ XPS core level components (P_1/P_2) have been plotted as a function of the emission angle for the (e) Ni and (f) Co core levels of the sample grown at 5 mT oxygen pressure and (g) Ni and (h) Co core levels of the sample grown at 30 mT oxygen pressure.

For both the NCO thin films prepared at the oxygen pressures of 5 mTorr and 30 mTorr, the binding energy differences between P_1 and P_2 components of the Ni and Co $2p_{3/2}$ core level spectra are 1.8 eV. Using ARXPS measurements, the ratios P_1/P_2 of both Ni and Co $2p_{3/2}$ core levels for the NCO thin film prepared at the oxygen pressure of 30 mTorr were, on average, found to increase as the emission angle increased with respect to the surface normal, indicating that P_1 (P_2) is a surface (bulk) weighted core level component. The NCO thin film prepared at the oxygen pressure of 30 mTorr has, therefore, surface-to-bulk weighted core level components that differ by about 1.8 eV in binding energies of the Ni and Co $2p_{3/2}$ core levels [33]. However, the dependence of the component intensity ratios (P_1/P_2) for the core levels on the emission angle was not found to be as significant, in the NCO thin film prepared at the oxygen pressure of 5 mTorr, as was the case in the NCO thin film prepared at the higher oxygen pressure of 30 mTorr, especially for the Co core level, as can be seen in figure 3(e)-(h). Any change in the oxygen pressure during sample growth might clearly affect the nature of the surface oxide and hence the dependency of the P_2/P_1 intensity ratios on the emission angle. The surface-to-bulk core level shift, in oxides in particular, may be due to differences in the chemical environments of the elements at the surface compared to the bulk [39]. Local environmental effects at the Ni and Co sites in NCO thin films might be altered by changes in the oxygen pressure during sample growth due to changes in the number of oxygen vacancies throughout the films. The diminished dependency of the P_2/P_1 ratios on the emission angle, for the NCO thin film prepared at the oxygen pressure of 5 mTorr, and hence little evidence for a surface-to-bulk core level shift, occurs with the film which is much more likely to be replete with oxygen vacancies throughout the entire film.

Due to the observed emission angle dependence of the relative intensities of the $2p_{3/2}$ core level component peaks of Ni and Co for NCO thin films, assigning features as surface weighted and bulk weighted is preferred in this work, rather than the usual assignments of the $2p_{3/2}$ core level components to multiple cationic species or to the presence of tetrahedral and octahedral sites. The assignments given to the $2p_{3/2}$ core level component peaks, typically for tetrahedral and octahedral sites, have a long history [1, 33] but do not seem to have a strong experimental validation. We have noticed that there is not even a prior general consensus on the physical interpretation of the component peaks in the core level spectra in the XPS of spinel oxides like NCO and CFO [33]. For instance, the component peak of Ni or Co $2p_{3/2}$ with lower binding energy (here labeled P_1 in this work) has been assigned to the +2oxidation state of the element in some reports, but other works suggest the same peak to be of +3 oxidation state [40–53]. Importantly, earlier XPS studies of the inverse spinel oxides have not given much attentions to the fact that photoemission, even core level photoemission, is surface sensitive and the surface may be distinct from the bulk. Here, ARXPS shows that, for both CFO and NCO thin films, there exist variations in the relative $2p_{3/2}$ component peaks with emission angle. The variations in the composition at the surface and bulk further indicate that the surface oxide is distinct from the bulk.

3.2. Evidence of non-metal to metal transitions at the surfaces of CoFe₂O₄(111) and NiCo₂O₄(111) thin films from temperature-dependent XPS

So far, in the above analyses of the ARXPS of both the CoFe₂O₄(111) and NiCo₂O₄(111) thin films, all the binding energies were corrected for any possible surface charging, that is, the surface photovoltaic effects mentioned at the outset have been taken into account. As we have indicated above, such corrections are always needed for insulating samples, in the absence of an external compensating current, usually implemented with a combination of a very low energy electron flood gun and ion sources. In the absence of an external compensating current, the photoemission process leads to a shift in the measured XPS core level binding energies as a result of the surface photovoltaic effect [2-4, 7, 55-60]. This surface charging resulting from the continuous photoemission-generated currents causes a misalignment of the effective Fermi levels between sample and the XPS spectrometer by some amounts equal to the photovoltaic surface charging (V), as illustrated in figure 4. Thus, the accumulated uncompensated surface charge leads to the apparent binding energy change of the core levels. For example, the XPS of a CFO thin film, in the geometry of our XPS system, showed the core level binding energy shifts by 5.8 eV, as shown in figure 4(c), indicating a large photovoltaic surface charging at the surface. The shift is consistent with the dielectric character of CFO. The XPS of NCO, for the same Mg K α (hv = 1253.6 eV) fluence, showed small shifts of around 0.4 ± 0.1 eV, suggesting that the prepared NCO thin films are significantly better conducting, compared to the CFO thin film. The core level binding energy, in XPS, is given by [61, 62]:

$$E_B^s = hv - KE_{sp} - \Phi_{sp}. \tag{3}$$

In equation (3), $E_{\rm B}^{\rm s}$ and KE_{sp} are the core level binding energy and the kinetic energy of the photoelectrons measured by the spectrometer, respectively, and $\Phi_{\rm sp}$ is the work function of the spectrometer. $E_{\rm B}^{\rm s}$ is measured with respect to the spectrometer's Fermi level ($E_{\rm F}^{\rm sp}$) which aligns with the Fermi level ($E_{\rm F}^{\rm s}$) of a sample only if the sample is sufficiently conducting. If a sample is insulating, the measured core level binding energy $E_{\rm B}^{\rm s}(T)$, at given temperature T, will be shifted by the photovoltaic surface charging V(T), as can be seen in figure 4(b), so that

$$E_{\rm B}^{\rm s}(T) = hv - KE_{sp} - \Phi_{\rm sp} + V(T).$$
 (4)

Hence

$$E_B^s(T) - E_B^s = V(T).$$
 (5)

So, the measured binding energy $E_{\rm B}^{\rm s}(T)$ at a temperature (T) is greater than the correct binding energy $(E_{\rm B}^{\rm s})$, which would be obtained in the absence of surface charging, by photovotaic charging V(T) at the temperature. With increasing temperature, carrier concentrations in the sample are expected to increase. With a sufficient carrier density in the sample, a

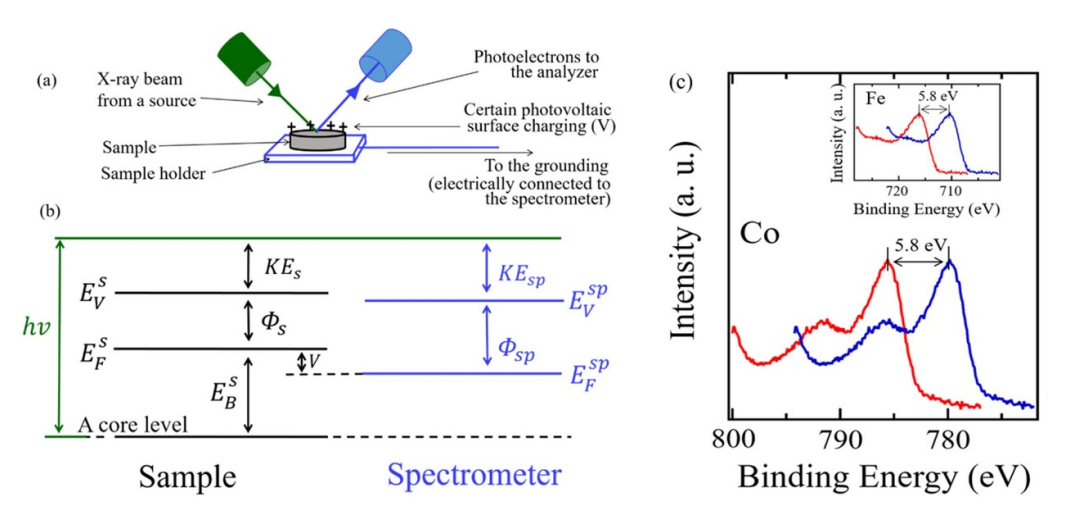


Figure 4. (a) A schematic of XPS experiment. The measured photoelectrons from well-defined core levels, resulting from the X-ray photon (hv) fluence, are only a small part of the photocurrent, which includes inelastically scattered and secondary photoelectrons. A (gray) sample is mounted on a metallic (rectangular) holder, which is in electrical contact with the XPS spectrometer. (b) The energy-level diagrams for the sample and the spectrometer showing the Fermi level misalignment for an insulating sample due to certain photovoltaic surface charging. The core level binding energy, Fermi level of sample (spectrometer), vacuum level of sample (spectrometer), work function of sample (spectrometer), and kinetic energy of photoelectron emitted from sample (as measured by spectrometer) are E_B^s , E_F^s (E_F^{sp}), E_V^s (E_V^{sp}), Φ_s (Φ_{sp}), and E_s (E_S^{sp}), respectively. (c) The Co (Fe in the inset) E_S^s (E_S^s) are the corrected spectra are the corrected spectra, corrected for the surface charging [54].

steady state charge compensation occurs through the sample and with sufficient conductivity throughout the sample, no surface charging occurs (in figure 4(b), V becomes zero) and hence the sample and spectrometer Fermi levels align. However, whether we can get $E_{\rm B}^{\rm s}(T)-E_{\rm B}^{\rm s}$ (or V(T)) truly equal to zero for a sample at some T remains a topic of debate [62-64].

The XPS core level spectra for CFO thin film illustrate this temperature-dependent surface photovoltaic effect, as seen in Co $2p_{3/2}$ and Fe $2p_{3/2}$ core level XPS spectra. Figure 5 shows temperature-dependent normal emission (emission angle is 0°) XPS for the CFO thin film. Starting at room temperature, the CFO thin film was annealed in stages to 605 K and the thin film was then cooled down to room temperature. It is evident that the XPS spectra of Co $2p_{3/2}$, Fe $2p_{3/2}$, and O 1s core levels show shifts in the apparent binding energies that are not symmetric with annealing and cooling, as shown in figure 5. Initially, at room temperature, the observed binding energies of all core levels were shifted from expected values by about 5.8 eV to larger binding energies by surface photovoltaic effects. This is not unexpected. The CFO thin film is an insulator at room temperature with an indirect (direct) band gap of $\sim 1.4 \text{ eV}$ ($\sim 2.5 \text{ eV}$) [65–79], and the intrinsic resistivity of CFO can be at least $\sim 10^3 \Omega$ cm [66, 78–80]. The core level binding energy shifts are therefore a very good indicator of photovoltaic surface charging during XPS measurements and hence the insulating nature of the prepared CFO thin film. As the sample temperature increases, the Co $2p_{3/2}$, Fe $2p_{3/2}$, and O 1s core level XPS binding energies decrease, indicating that surface charging decreases with increasing temperature. The changes in the XPS core level binding energies cease at around 455 K as shown in figure 5. Such changes in the measured core level binding energies of the Co $2p_{3/2}$, Fe $2p_{3/2}$, and O 1s were observed to be irreversible with temperature. When the sample temperature decreased from 605 K back to room temperature, the core level binding energies of CFO did not change, making the temperature-dependent XPS binding energy changes irreversible under ultra-high vacuum conditions and indicating that the sample became and remained more conducting after annealing the sample at higher temperatures. The trend of the temperature-dependent changes in core level binding energies of CFO suggests that the annealing of CFO thin films in ultra-high vacuum conditions leads to irreversible insulating (non-metallic) to conducting (metallic) transition (in vacuum) when temperature is increased.

Based on the temperature-dependent photovoltaic charging signatures of the XPS binding energies, the NCO thin film is also observed to undergo an irreversible transition with temperature, but the character of this transition is different from that seen with CFO thin film. To investigate the temperaturedependent properties of NCO thin films, we selected films prepared at the lower oxygen pressure of 5 mTorr because, for these NCO thin films, there are a larger number of oxygen vacancies; however, the samples are still more conducting at the outset than CFO and likely more easily driven through the metal to non-metal phase transition. In addition, the ARXPS indicates that the NCO surface more closely resembles the bulk (for the NCO samples prepared at lower oxygen pressure of 5 mT) than is the case for CFO and NCO prepared at a higher oxygen pressure, as discussed above. Figure 6 shows the temperature-dependent Ni $2p_{3/2}$, Co $2p_{3/2}$, and O 1s XPS core level spectra taken at normal emission and the binding energies of corresponding core level features, as a function of temperature, for the NCO thin films prepared at the oxygen pressure of 5 mTorr. During the initial increase in the temperature of the NCO thin film, there is little or no appreciable

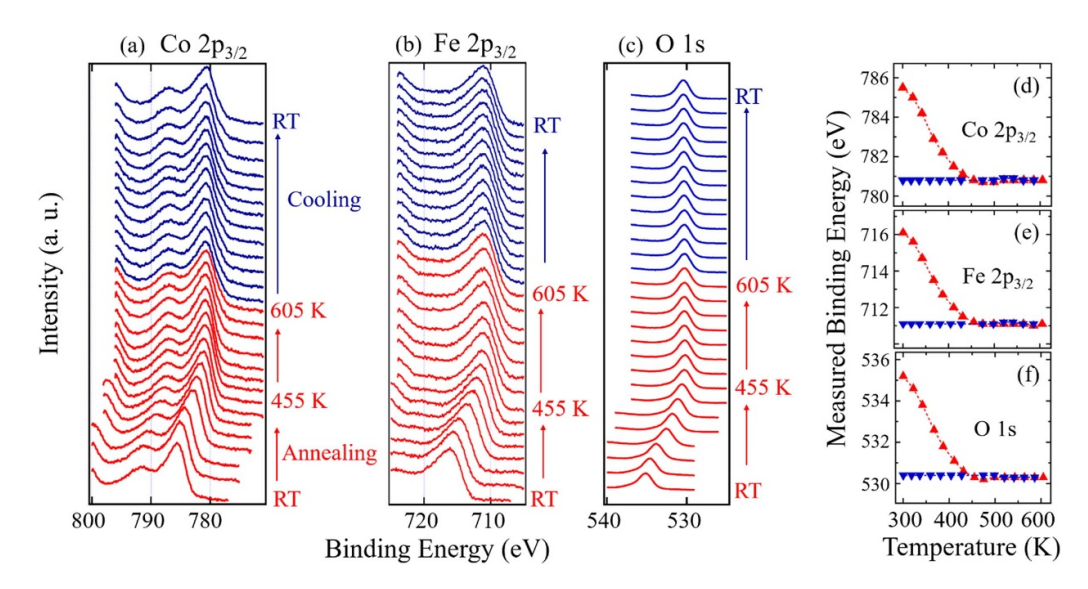


Figure 5. The temperature-dependent Co $2p_{3/2}$, Fe $2p_{3/2}$, and O 1s core level XPS spectra taken at normal emission for a CoFe₂O₄(111) (CFO) thin film. The (a) Co $2p_{3/2}$, (b) Fe $2p_{3/2}$, and (c) O 1s core level XPS spectra of CFO are shown at different temperatures during annealing (red spectra) and cooling (blue spectra) cycles. The measured binding energies of the (d) Co $2p_{3/2}$, (e) Fe $2p_{3/2}$, and (f) O 1s core level main peaks have been plotted as a function of temperature during annealing (red upright triangles) and cooling (blue inverted triangles) cycles. RT indicates room temperature (roughly 297 K).

changes in the measured core level binding energies. It has already been noted elsewhere that depending upon the sample growth conditions and distribution of cationic species, the prepared NCO thin film can be conducting and exhibit resistivities as low as $\sim 10^{-3}~\Omega$ cm at room temperature [27, 81–106]. The absence of discernible core level binding energy changes, with increasing temperature during the first annealing treatment, is consistent with the conducting nature of the NCO thin films. This initial annealing treatment, under ultra-high vacuum conditions, of the NCO thin films prepared at the lower oxygen pressure of 5 mTorr, however, does change the nature of the film.

The temperature dependence of the NCO thin film core level binding energies became evident when the NCO thin film, prepared at the oxygen pressure of 5 mTorr, was cooled from 591 K to room temperature (297 K) after the initial annealing treatment. The changes in the XPS core level binding energies with temperature were observed to be reversible with temperature in this new phase, with strong photovoltaic charging occurring at lower temperatures and with the measured core level binding energies decreasing at higher temperatures, as shown in figure 6. A small hysteresis was observed between cooling and 2nd annealing cycles for the NCO thin film core level binding energy changes with temperature. For NCO, the temperature-dependent core level shifts are more dramatic, since the maximum changes in the measured core level binding energies of Ni $2p_{3/2}$, Co $2p_{3/2}$, and O 1s were found to be about 6.4 eV, 7.0 eV, and 6.9 eV respectively, which are significantly larger than the binding energy changes observed for the initial dielectric phase of CFO, as discussed above and plotted in figure 5.

Based on the behavior of the photovoltaic charging, of the core level XPS binding energies, both CFO and NCO thin films have clearly undergone a phase transition in the first

annealing cycle under ultra-high vacuum conditions. Since the as-prepared CFO was an insulator, there was initially temperature-dependent surface charging when the CFO was annealed. The annealing process, however, led to a non-metal to metal phase transition for CFO, as discussed above, so that there were no changes in core level binding energies, with temperature, for the latter conducting phase of CFO, as was also seen with the initial conducting phase of the NCO thin film during the first annealing cycle. The initially conducting NCO thin film became an insulator when annealed, subsequently exhibiting temperature-dependent behavior of the core level binding energies during cooling and second annealing cycles, indicative of a non-conducting or insulating phase, as shown in figure 6. Thus, the CFO thin film can be driven from an insulating to a conducting phase, whereas the NCO thin film can be driven from a conducting to an insulating phase upon annealing in vacuum. The phase changes of both the CFO and NCO thin films are irreversible with temperature. Interestingly, when the NCO thin film became insulator (or non-metal) after the first annealing treatment, reversible core level binding energy changes were observed with temperature (with cooling and second annealing cycles as shown in figure 6). Since the phase transition processes were not reversed upon cooling the CFO and NCO thin films back to room temperature, thermally generated electron and hole carriers at higher temperatures cannot be the sole source for the surface photovoltage compensation. The irreversible insulating (non-metallic) to conducting (metallic) transition (in vacuum) for CFO suggests that there should be defect or vacancy formation at the CFO thin film surface at elevated temperatures. The same may be said for the irreversible conducting (metallic) to insulating (non-metallic) transition (in vacuum) seen for NCO thin film, prepared at a lower oxygen pressure of 5 mTorr, which exhibits hysteresis in the reversible changes

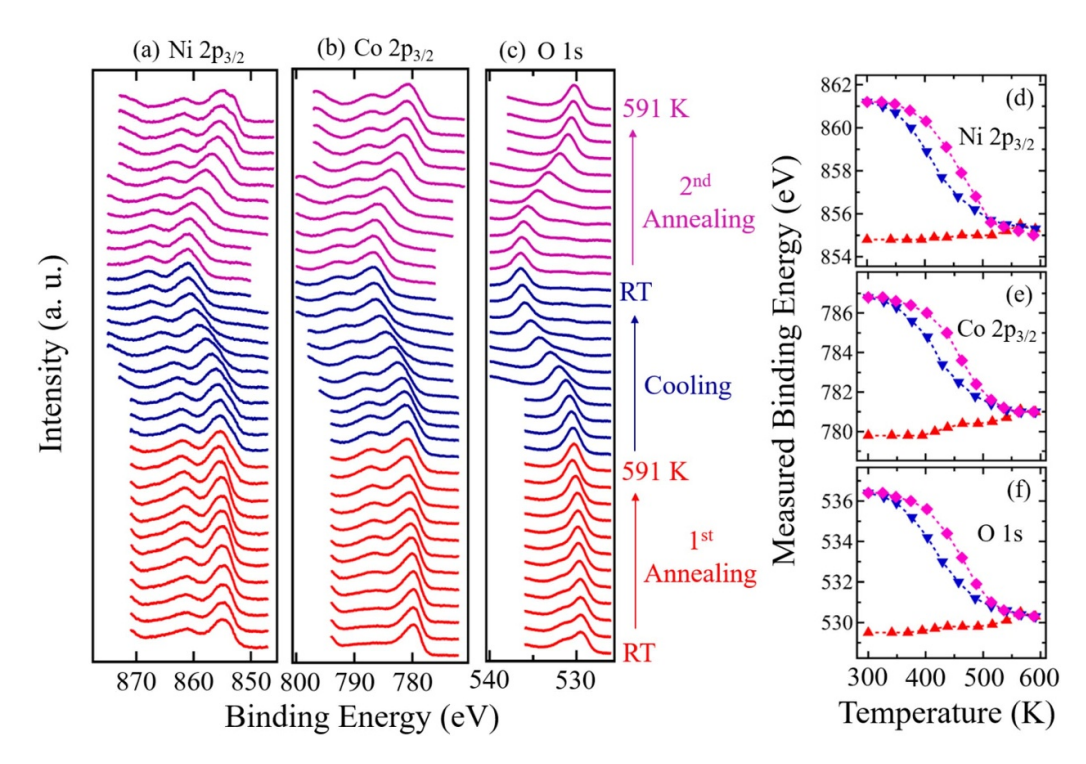


Figure 6. The temperature-dependent Ni $2p_{3/2}$, Co $2p_{3/2}$, and O 1s core level XPS spectra taken at normal emission for a NiCo₂O₄(111) (NCO) thin film grown at 5 mT oxygen pressure. The (a) Ni $2p_{3/2}$, (b) Co $2p_{3/2}$, and (c) O 1s core level XPS spectra of NCO at different temperatures during first annealing (red spectra), cooling (blue spectra) and second annealing (violet spectra) cycles are shown. The measured binding energies of the (d) Ni $2p_{3/2}$, (e) Co $2p_{3/2}$, and (f) O 1s core level main peaks are plotted as a function of temperature during first annealing (red upright triangles), cooling (blue inverted triangles) and 2nd annealing (violet diamonds) cycles. RT indicates room temperature (roughly 297 K).

in the XPS core level binding energy changes once in the insulating (non-metallic) phase. Furthermore, thermally generated electron and hole carriers at higher temperatures cannot explain the noticeable deformation (figure S2 in SI) of core level spectra observed for the NCO thin film at higher temperatures.

3.3 The possible role of oxygen vacancies in mediating the non-metal to metal transitions at the surfaces of $CoFe_2O_4(111)$ and $NiCo_2O_4(111)$ thin films with temperature

Vacancy formation through the loss of oxygen atoms with increasing temperature, from the surface of oxide thin films, is expected [11]. In high-temperature XPS measurements, photoelectron and secondary electron currents, combined with higher temperatures, may enhance oxygen loss from oxide thin films. Oxygen atoms leaving from the surface result in the chemical reduction of the specimen and increase of the n-type character of an insulator or semiconductor. The availability of additional electrons and the reduction of cationic species due to oxygen vacancies at higher temperatures should play important roles in the observed variations in binding energy changes with temperature and the electronic phase changes of the CFO and NFO films.

We have used XPS to investigate whether oxygen vacancies play some role in the insulating (non-metallic) to conducting (metallic) transition for CFO and conducting (metallic) to insulating (non-metallic) transition for NCO films and the temperature-dependent surface charging in CFO and NCO films. Figure 7 shows the Co $2p_{3/2}$, Fe $2p_{3/2}$, and O 1s core level XPS spectra of the CFO thin film after vacancy creation through annealing followed by oxygen exposure treatments. The first (i) and the second (ii) Co $2p_{3/2}$, Fe $2p_{3/2}$, and O 1s core level spectra at the bottom of figure 7(a)–(c) were acquired at room temperature and while annealing the thin film at 605 K, respectively (see also figure 5). Going from room temperature to 605 K, there were changes in the Co $2p_{3/2}$, Fe $2p_{3/2}$, and O 1s core level binding energies for the CFO thin film surface, as noted above, but does annealing of the sample in oxygen change the observed shifts back to higher binding energies, caused by surface photovoltage effects, at room temperature?

Annealing the CFO thin film at low oxygen pressure causes some changes to the Co $2p_{3/2}$, Fe $2p_{3/2}$, and O 1s core level spectra. The sample was later annealed at 574 K in the oxygen pressure of 5×10^{-6} Torr, and XPS spectra were acquired, as shown in the (iii) spectra of figure 7. Increases in the binding energies (main peak positions) of the Co $2p_{3/2}$, Fe $2p_{3/2}$, and O 1s core level features were observed, indicating that oxidation increased the photovoltaic surface charging and hence the insulating properties of the CFO thin film surface region. The shapes of the CFO thin film Co $2p_{3/2}$, Fe $2p_{3/2}$, and O 1s XPS core level spectra were, however, not restored and some XPS core level components were observed as shown (iii) spectra in figure 7, which resulted in spectral shapes with some deformations and deviations from what is expected [1, 36, 37].

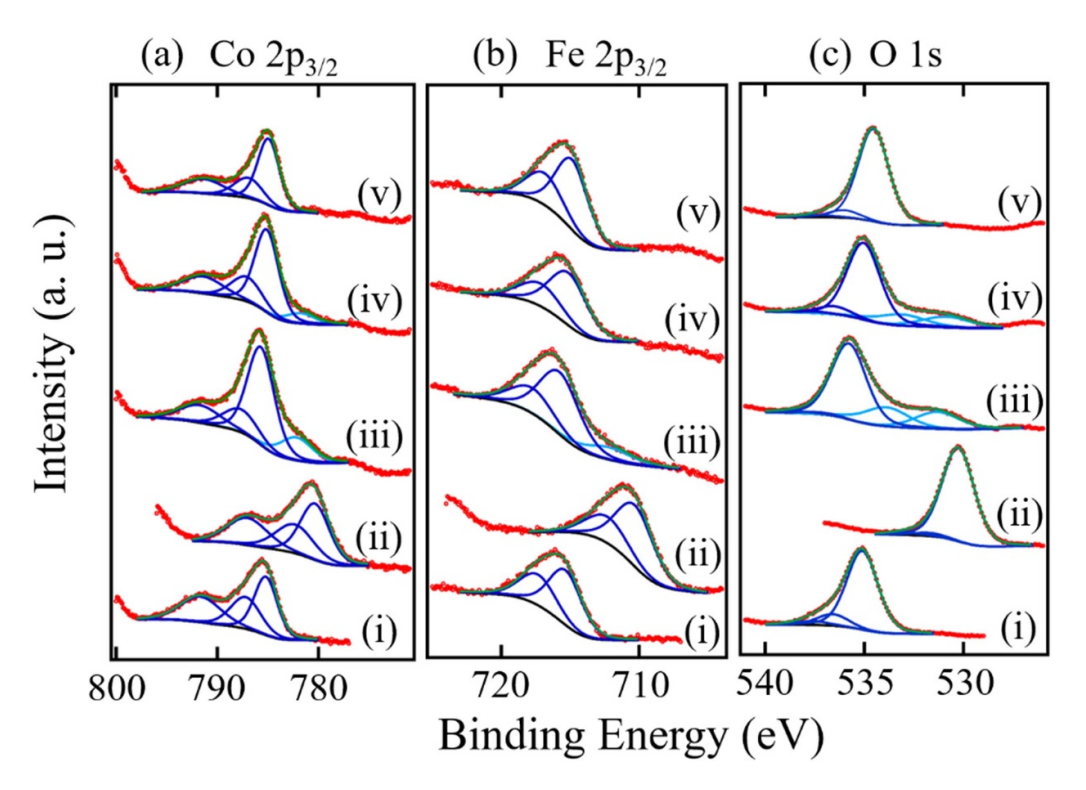


Figure 7. The Co $2p_{3/2}$, Fe $2p_{3/2}$, and O 1s core level XPS spectra taken at normal emission for CoFe₂O₄(111) (CFO) under different conditions. (a) Co $2p_{3/2}$, (b) Fe $2p_{3/2}$, and (c) O 1s XPS core level spectra are shown for CFO (i) at room temperature just before annealing, (ii) at 605 K, (iii) after the sample was annealed at 574 K in oxygen pressure of 5×10^{-6} Torr, (iv) after the sample was exposed to ambient conditions, and (v) after the sample was annealed in ambient oxygen pressure. The component peaks, shown in blue solid are expected for inverse spinel oxides, whereas the components in cyan blue may be assigned to residual surface domains of more metallic CFO or a more reduced oxide. The higher binding energy components of O 1s spectra represent surface contamination species (see also figure S4 of SI) [107].

The spectral deformations are likely the results of residual surface domains of a more metallic CFO or possibly a more reduced surface oxide.

After acquiring the (iii) XPS spectra (figure 7), then exposing the CFO thin film to ambient conditions for several hours, the XPS spectra (iv) taken for the Co $2p_{3/2}$, Fe $2p_{3/2}$, and O 1s core levels, shown in figure 7, showed some reduction of the features characteristic of more metallic surface domains or a more reduced oxide. Annealing the sample in ambient oxygen (the XPS spectra (v) in figure 7) seems to eliminate the lower binding energy components (components in cyan blue), and the XPS core level spectra become restored to what were initially observed. Furthermore, the Co $2p_{3/2}$ satellite feature, at higher binding energy, has diminished intensity relative to the other Co $2p_{3/2}$ components, which is often indicative of a reduction in the number of oxygen vacancies suggesting that the number of oxygen vacancies is reduced with the various oxygen treatments, driving the CFO surface more dielectric, consistent with the increased photovoltaic charging. Taken as a whole, this shows that the number of oxygen vacancies at the surface can affect the binding energies of the core level spectra and hence the sample charging in XPS measurements, as shown in figures 5 and 7.

Similar annealing and oxygen exposure experiments were conducted for the NCO thin film to validate that oxygen vacancies play a role in binding energies of the Ni $2p_{3/2}$, Co $2p_{3/2}$,

and O 1s XPS core level peaks. In figure 8, the core level XPS spectra at room temperature (i) are shown in comparison with the XPS spectra obtained after annealing and oxygen exposure of NCO thin film. The room temperature XPS core level spectra after the first annealing and the cooling cycles are shown in the (ii) spectra of figure 8, and the (iii) spectra were taken at 591 K during the second annealing cycle of NCO (see also figure 6). The Ni $2p_{3/2}$ and Co $2p_{3/2}$ XPS core level spectra of NCO, taken at 591 K during second annealing cycle, have significant spectral contributions at lower binding energies characteristic of more reduced surface oxides. The low binding energy XPS core level components characteristic of reduced oxides, in the XPS Ni and Co $2p_{3/2}$ core level spectra, increased during the second annealing cycle (figure S3 in SI) and we attribute this to an increase in oxygen defect concentration at the surface. The XPS spectral components associated with the reduced oxides diminished significantly when the NCO sample was exposed to ambient conditions, as shown in the (iv) spectra of figure 8. The NCO thin film was observed to be insulator even after exposing it to ambient conditions, with high photovoltaic surface charging, indicated by the XPS core level peak (binding energy) shifts in the (iv) spectra of the figure 8. The original XPS core level spectral shapes and binding energies of the core levels were restored when the sample was annealed in ambient oxygen, as shown in (v) spectra of figure 8. This means that the NCO thin films become insulators

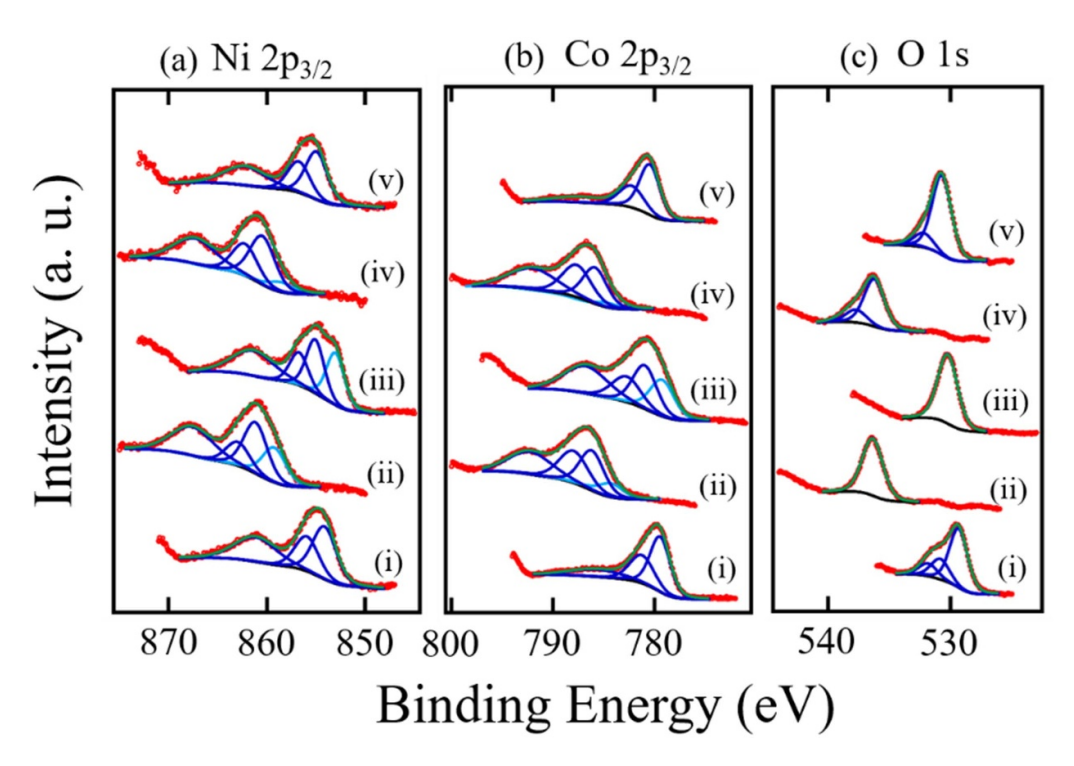


Figure 8. The Ni $2p_{3/2}$, Co $2p_{3/2}$ and O 1s core level XPS spectra taken at normal emission for NiCo₂O₄(111) (NCO) under different conditions. The XPS spectra are shown of the (a) Ni $2p_{3/2}$, (b) Co $2p_{3/2}$, and (c) O 1s core levels (i) at room temperature just before annealing, (ii) at room temperature after 1st annealing and the cooling, (iii) at 591 K during the second annealing step, (iv) after the sample was exposed to ambient conditions, and (v) after the sample was annealed in ambient oxygen pressure. The spectral component peaks in blue are expected for inverse spinel oxides, whereas the components in cyan blue are attributable to more reduced oxides. The higher binding energy components of O 1s represent surface contamination species (see also figure S4 of SI) [107].

when oxygen defects are introduced, but for the NCO sample to be more conducting again at room temperature, the sample needs to be oxidized heavily. Our results align with the findings that oxygen vacancies open the band gap in the density of state calculations of NCO [38] and decrease in Ni³⁺ ions (reduction of Ni in this work) leads to increased insulating character of NCO films [38, 86]. This is diametrically different from CFO thin films where oxygen vacancies lead to increase in conductivity and to a non-metal to metal transition, as discussed above.

Redox reactions, that is to say an increase or decrease in the number of oxygen vacancies, can lead to a change in the majority carrier and conductance in oxides [108, 109]. It has long been recognized that the band bending and the associated photovoltaic charging are different for n-type versus ptype semiconductors [110-112], which lead to shifts in the core level binding energies. Our results cannot be explained solely on the basis of the band bending analysis as the change in core level binding energy observed is much greater than the band gap. For instance, the core level binding energy change for CFO is about 5 eV, but the indirect (direct) band gap is around $\sim 1.4 \text{ eV}$ ($\sim 2.5 \text{ eV}$) [65–77]. In this work, the major underlying phenomenon causing the core level binding energy to change with temperature is the presence or absence of charge compensation and Fermi level alignment between sample and spectrometer. The band at the sample surface can bend, leading to binding energy shifts. These shifts cannot exceed the band gap [110–112]. Furthermore, the studies of changing oxygen concentration at the oxide surface [108, 109] tend to support our observation of decrease in surface charging (or increase in conductance) due to reduction at the surface for the $CoFe_2O_4(111)$ thin film.

3.4. A model for temperature-dependent core level binding energy change or surface charging

From the temperature-dependent core level XPS binding energies of insulating CFO and insulating NCO thin films, as seen in figures 5(d)-(f) and 6(d)-(f), an estimate of the carrier activation energy may be obtained. At room temperature, the core level binding energies in XPS of a dielectric oxide thin film are shifted to high binding energies due to surface charging and perhaps due to a very minor extent by band bending as discussed above. As the temperature is increased, the electron carrier concentration should increase due to the thermal excitation of trapped electrons and additional number of electron carriers due to the surface reduction (loss of oxygen). The availability of electrons to the surface decreases the surface charging and hence the core level binding energies in higher temperature XPS. Both the excitation of trapped electrons and oxygen vacancy creation are activated processes. The change in core level binding energy with temperature in this work should have a mathematical model similar to the model (the Arrhenius equation) for temperature dependence of conductivity in semiconductors. Figure 9 shows the plots for a possible model of temperature-dependent XPS core level binding energies of

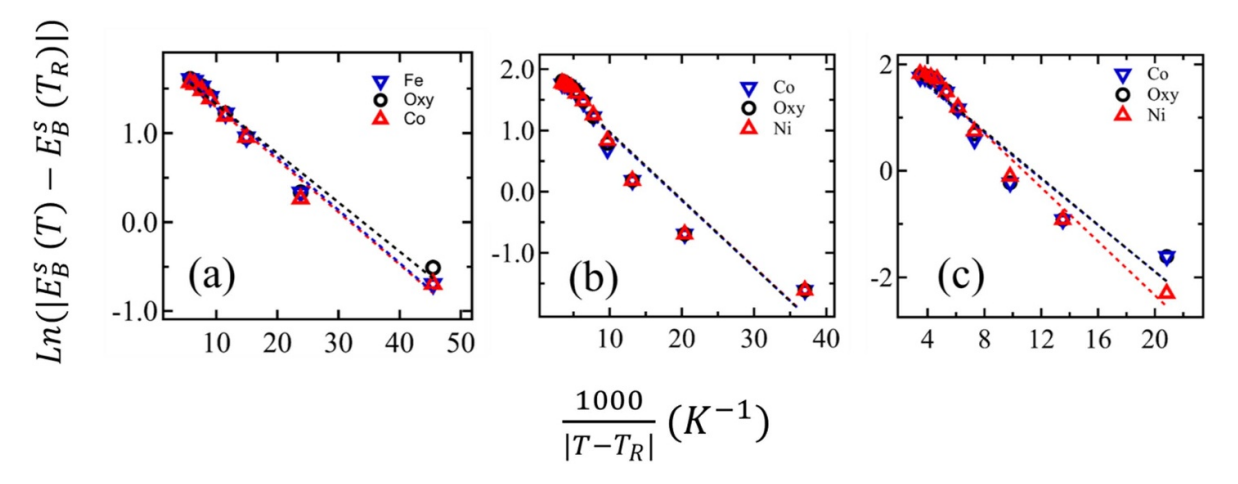


Figure 9. The logarithmic plots of $|E_B^s(T) - E_B^s(T_R)|$ vs $\frac{1}{|T - T_R|}$ during (a) the annealing of insulating CoFe₂O₄(111) (CFO) thin film, (b) the cooling of insulating NiCo₂O₄(111) (NCO) thin film from 605 K, and (c) 2nd annealing of insulating NCO thin film. $E_B^s(T)(E_B^s(T_R))$ are the core level binding energy at temperature $T(T_R)$, room temperature).

Table 1. The activation energies (E_a) and coefficients of determination $(r^2$ values) using the best fit. A perfect functional model has r^2 value of 1.

The core level of	Activation energy E_a (J mol ⁻¹)	Coefficient of determination $(r^2 \text{ value})$ for the fitted line
For CoFe ₂ O ₄ (During	g heating)	
Co	489 ± 18	0.98
Fe	494 ± 15	0.99
Oxygen	459 ± 19	0.98
For NiCo ₂ O ₄ (During	g cooling)	
Ni	913 ± 74	0.94
Co	910 ± 76	0.94
Oxygen	920 ± 76	0.94
For NiCo ₂ O ₄ (During	g 2nd heating)	
Ni	2103 ± 98	0.98
Co	1808 ± 170	0.93
Oxygen	1830 ± 170	0.94

insulating CFO and NCO thin films. We present a very good linear least squares fit of the logarithmic part of the absolute value of the core level binding energy change relative to the core level binding energy at room temperature (T_R), as a function of the inverse of the absolute value of the temperature change from room temperature, as expressed by the following modified Arrhenius-type [113] equation:

$$|\Delta BE| = A \exp\left[\frac{-E_a}{R|\Delta T|}\right]$$
 (6)

where $\Delta BE = E_B^s(T) - E_B^s(T_R)$ and $\Delta T = T - T_R$. In equation (6), E_a is the activation energy and A is the pre-exponential frequency factor, which is assumed here to be independent of temperature and effectively a constant. Since ΔBE is defined with respect to room temperature, the absolute value of core level binding energy change (ΔBE) in equation (6) increases as the temperature change (ΔT)

increases from room temperature, which is expected behavior between dependent and independent variables in Arrheniustype equation.

Deviations of the plots of the logarithm of the change in the core level binding energy versus the inverse of the change in temperature, as shown in figure 9, from the perfect linear nature, are not entirely unexpected. The change in conductance of NCO and CFO with temperature is not only due to the increased carrier concentration with increasing temperature but also due to the change in carriers associated with increased oxygen vacancy formation at higher temperatures. These two processes occur simultaneously, but likely with different activation energies. Thus, we extract from the core level binding energy shifts with temperature an effective activation energy for changing conductance that includes both processes. Deviations from the perfect linear nature, in figure 9, are, however, small as the r^2 values for the fitting are still very close to 1.

Table 1 lists the effective activation energies and coefficients of determination (r^2) for the model expressed by equation (6). Values of r^2 close to unity suggest that the core level binding energy changes, and hence the photovoltaic surface charging, of insulating CFO and NCO thin films in temperature-dependent XPS follow the proposed model expressed by (6).

Table 1 shows that relatively lower activation energies for the core levels of CFO thin films, compared to the NCO thin films, are observed. This finding suggests that carrier creation and surface oxygen loss at the surface of CFO are more facile than for NCO. For NCO, we observed that the activation energies extracted from the surface photovoltaic charging are doubled for second annealing compared to cooling. Higher activation energies for the second annealing of NCO suggest that carrier generation during the second annealing required higher energies. The higher thermal energy, required to create carriers to compensate the photovoltaic surface charging when the NCO film was annealed for the second time, may be the result of increased oxygen loss, but also suggests that the defect states within the band gap are farther from the band edges. Different surface defect densities created and different activation energies for the cooling and for the second annealing cycles of NCO thin film should account for the observed hysteresis in the measured binding energy vs temperature in figure 6.

4. Conclusions

Although both CFO and NCO thin films are inverse spinels, annealing the thin films in vacuum drives a CFO thin film from non-metallic (insulating or dielectric) to metallic (conducting) and a NCO thin film from metallic (conducting) to nonmetallic (insulating or dielectric). Both thermally generated electron and hole carriers and oxygen vacancies play important roles in temperature-dependent photovoltaic surface changing, observed in both CFO and NCO thin films. The increase in oxygen vacancies plays a major role in electronic phase transitions of CFO and NCO thin films, leading to increased insulating character for NCO films, that is a metal to non-metal transition. In contrast, for CFO thin films, oxygen vacancies increase conducting character and lead to a non-metal to metal transition. The fact that the properties observed in one oxide may differ in another oxide is further established here, and it would be difficult to generalize the non-metal to metal transition at the surface of one oxide to another. Furthermore, not only is the apparent surface-to-bulk core level shift possibly due to the surface oxide being different from the bulk, but it is now also clear that there may be an interplay between surface segregation and the surface of the oxide.

 ${\rm CoFe_2O_4}$ and ${\rm NiCo_2O_4}$ thin films have often been mentioned in the context of spintronics. The new insight that metal-to-insulator transition (MIT) can also be applied to these materials opens an avenue for defect assisted and/or temperature-dependent future beyond CMOS devices. In particular, the insulating phase for ${\rm NiCo_2O_4}$ thin film can undergo reversible MIT even in a redox programmable

devices and this redox could be voltage controlled and thus "programmable." The non-metal to metal transition seen for CoFe₂O₄(111) and NiCo₂O₄(111) thin films could well be localized just to the surface regions opening the door for an Anderson-type temperature dependent field effect transistor unlike the Mott transistor schemes proposed [114–117].

For CFO and NCO in the insulating phase, our studies suggest that the core level binding energies, measured by XPS technique, and hence the surface charging, follow a model, as a function of temperature, given by $|\Delta BE| = A \exp\left[\frac{-E_a}{R|\Delta T|}\right]$.

Data availability statement

All data that support the findings of this study are included within the article (and any supplementary files).

Acknowledgments

A Subedi acknowledges Archit Dhingra for some useful discussion. This work was supported by the Nebraska Public Power District through the Nebraska Center for Energy Sciences Research at the University of Nebraska-Lincoln and National Science Foundation (NSF) through the EPSCoR RII Track-1: Emergent Quantum Materials and Technologies (EQUATE), Award No. OIA-2044049.

Author contributions

Sample preparation: D Y and X X; data acquisition: A S and D Y; data analysis: A S; data curation: A S and P A D; manuscript preparation: A S; final manuscript preparation: A S and P A D; project supervision: X X and P A D; funding: X X and P A D

Conflict of interest

There are no conflicts to declare.

ORCID iDs

Arjun Subedi https://orcid.org/0000-0002-7581-8144 Xiaoshan Xu https://orcid.org/0000-0002-4363-392X Peter A Dowben https://orcid.org/0000-0002-2198-4710

References

- [1] Subedi A, Yang D, Yun Y, Xu X and Dowben P A 2022 J. Vac. Sci. Technol. A 40 023201
- [2] Baer D R, Artyushkova K, Cohen H, Easton C D, Engelhard M, Gengenbach T R, Greczynski G, Mack P, Morgan D J and Roberts A 2020 J. Vac. Sci. Technol. A 38 031204
- [3] Tasci T O, Atalar E, Demirok U K and Suzer S 2008 Surf. Sci. 602 365–8
- [4] Ertas G, Demirok U K, Atalar A and Suzer S 2005 Appl. Phys. Lett. 86 183110
- [5] Cazaux J 1999 J. Electron Spectros. Relat. Phenomena 105 155–85

- [6] Cazaux J 2000 J. Electron Spectros. Relat. Phenomena 113 15–33
- [7] Tielsch B J, Fulghum J E and Surman D J 1996 Surf. Interface Anal. 24 459–68
- [8] Dugan C, Hengehold R L, McHale S R, Colón Santana J A, McClory J W, Adamiv V T, Burak Y V, Losovyj Y B and Dowben P A 2013 Appl. Phys. Lett. 102 161602
- [9] Wang Z, Lin R, Huo Y, Li H and Wang L 2022 Adv. Funct. Mater. 32 2109503
- [10] Ganduglia-Pirovano M V, Hofmann A and Sauer J 2007 Surf. Sci. Rep. 62 219–70
- [11] Sarkar A and Khan G G 2019 Nanoscale 11 3414-44
- [12] Kevane C J 1964 Phys. Rev. 133 A1431
- [13] Kılıç C and Zunger A 2002 Phys. Rev. Lett. 88 955011-4
- [14] Diebold U, Li M, Dulub O, Hebenstreit E L D and Hebenstreit W 2000 Surf. Rev. Lett. 7 613–7
- [15] Morant C, Sanz J M and Galãn L 1992 Phys. Rev. B 45 1391–8
- [16] Wang Z, Mao X, Chen P, Xiao M, Monny S A, Wang S, Konarova M, Du A and Wang L 2019 Angew. Chem. 131 1042–6
- [17] Blum R P, Niehus H, Hucho C, Fortrie R, Ganduglia-Pirovano M V, Sauer J, Shaikhutdinov S and Freund H-J 2007 Phys. Rev. Lett. 99 226103
- [18] Wang Q, Puntambekar A and Chakrapani V 2016 *Nano Lett.* **16** 7067–77
- [19] Nili H et al 2016 Nanotechnology 27 505210
- [20] Tang K, Meng A C, Hui F, Shi Y, Petach T, Hitzman C, Koh A L, Goldhaber-Gordon D, Lanza M and McIntyre P C 2017 Nano Lett. 17 4390–9
- [21] Wang J, Wang Z, Huang B, Ma Y, Liu Y, Qin X, Zhang X and Dai Y 2012 ACS Appl. Mater. Interfaces 4 4024–30
- [22] Dong F, Xiao X, Jiang G, Zhang Y, Cui W and Ma J 2015 Phys. Chem. Chem. Phys. 17 16058–66
- [23] Triolo C, Schweidler S, Lin L, Pagot G, Di Noto V, Breitung B and Santangelo S 2023 Energy Adv. 2 667
- [24] Fujii K, Sato Y, Takase S and Shimizu Y 2015 *J. Electrochem. Soc.* 162 F129–35
- [25] Gayen P, Saha S, Bhattacharyya K and Ramani V K 2020 ACS Catal. 10 7734–46
- [26] Yang D, Yun Y, Subedi A, Rogers N E, Cornelison D M and Dowben P A 2021 Phys. Rev. B 103 224405
- [27] Xu X, Mellinger C, Cheng Z G, Chen X and Hong X 2022 J. Appl. Phys. 132 020901
- [28] Jauhar S, Kaur J, Goyal A and Singhal S 2016 RSC Adv. 6 97694–719
- [29] Mellinger C, Wang X, Subedi A, Clark A T, Komesu T, Rosenberg R, Dowben P A, Cheng X and Xu X 2023 J. Appl. Phys. 133 195301
- [30] Cheng R, Xu B, Borca C N, Sokolov A, Yang C S, Yuan L, Liou S H, Doudin B and Dowben P A 2001 Appl. Phys. Lett. 79 3122–4
- [31] Dulli H, Dowben P A, Liou S H and Plummer E W 2000 Phys. Rev. B 62 R14629–32
- [32] Borca C N, Xu B, Komesu T, Jeong H, Liu M T, Liou S H and Dowben P A 2002 Surf. Sci. Lett. 512 L346–52
- [33] Subedi A et al 2024 J. Phys.: Condens. Matter 36 285001
- [34] Dowben P A and Miller A 1990 Boca (CRC Press)
- [35] Mcintyre N S and Cook M G 1975 Anal. Chem. 47 2208–13
- [36] McIntyre N S and Zetaruk D G 1977 Anal. Chem. 49 1521–9
- [37] Cheng J, Lu Y, Qiu K, Yan H, Xu J, Han L, Liu X, Luo J, Kim J-K and Luo Y 2015 Sci. Rep. 5 12099
- [38] Huang X C et al 2021 Phys. Rev. B 104 125136
- [39] Spanjaard D, Guillot C, Desjonqueres M C, Treglia G and Lecante J 1985 *Surf. Sci. Rep.* **5** 1–85
- [40] Lee J H, Noh Y W, Jin I S, Park S H and Jung J W 2019 J. Mater. Chem. C 7 7288–98
- [41] Liu Y, Chi X, Han Q, Du Y, Yang J and Liu Y 2019 J. Alloys Compd. 772 693–702

- [42] Ouyang D, Xiao J, Ye F, Huang Z, Zhang H, Zhu L, Cheng J and Choy W C H 2018 Adv. Energy Mater. 8 1702722
- [43] Waghmode R B, Maile N C, Lee D S and Torane A P 2020 Electrochim. Acta 350 136413
- [44] Marco J F, Gancedo J R, Gracia M, Gautier J L, Ríos E I, Palmer H M, Greaves C and Berry F J 2001 J. Mater. Chem. 11 3087–93
- [45] Wang S, Wang L, Liu C, Shan Y, Li F and Sun L 2022 RSC Adv. 12 12544–51
- [46] Kang P, Zhou G, Ji H, Li Z, Li Z and Xu X 2022 J. Magn. Magn. Mater. 553 169293
- [47] Wang W, Du Q, Wang B, Li Y, Hu Z, Wang Y, Wang Z and Liu M 2022 J. Appl. Phys. 132 073901
- [48] Zhang R, Liu M, Liu W and Wang H 2017 Mater. Lett. 199 164-7
- [49] Li L, Ma Z, Liu L, Wang X, Wang J, Cao L Y, Liu S and Zhang W 2022 Mater. Res. Bull. 145 111528
- [50] Bacelis-Martínez R D, Oskam G, Rodriguez Gattorno G and Ruiz-Gómez M A 2017 Adv. Mater. Sci. Eng. 2017 9647458
- [51] Liu Z, Zhen C, Xu D, Wu X, Wang H, Ma L, Zhao D, Tian Z and Hou D 2020 Appl. Surf. Sci. 529 147155
- [52] Liu J, Meng R, Li J, Jian P, Wang L and Jian R 2019 Appl. Catal. B 254 214–22
- [53] Gao M, Le K, Du W, Wang Z, Wang F, Liu W and Liu J 2019 New J. Chem. 43 13491–8
- [54] Barr T L and Seal S 1995 J. Vac. Sci. Technol. A 13 1239-46
- [55] Cros A 1992 J. Electron Spectros. Relat. Phenomena 59 1-14
- [56] Villar-Garcia I J, Smith E F, Taylor A W, Qiu F, Lovelock K R J, Jones R G and Licence P 2011 Phys. Chem. Chem. Phys. 13 2797–808
- [57] Tielsch B J and Fulghum J E 1996 *Surf. Interface Anal.* **24** 422–7
- [58] Wooten D, Ketsman I, Xiao J, Losovyj Y B, Petrosky J C, McClory J, Burak Y, Adamiv V and Dowben P A 2009 MRS Online Proc. Libr. 1164 1164–L04–04
- [59] Xiao J et al 2011 Appl. Surf. Sci. 257 3399-403
- [60] Barr T L 1989 J. Vac. Sci. Technol. A 7 1677–83
- [61] Stevie F A and Donley C L 2020 J. Vac. Sci. Technol. A 38 063204
- [62] Greczynski G and Hultman L 2020 Prog. Mater. Sci. 107 100591
- [63] Greczynski G and Hultman L 2021 Sci. Rep. 11 11195
- [64] Greczynski G and Hultman L 2018 Appl. Surf. Sci. 451 99–103
- [65] Sharma D and Khare N 2014 Appl. Phys. Lett. 105 032404
- [66] Rai R C, Wilser S, Guminiak M, Cai B and Nakarmi M L 2012 Appl. Phys. A 106 207–11
 [67] Himcinschi C, Vrejoiu I, Salvan G, Fronk M,
- [67] Himcinschi C, Vrejoiu I, Salvan G, Fronk M, Talkenberger A, Zahn D R T, Rafaja D and Kortus J 2013 J. Appl. Phys. 113 084101
- [68] Fritsch D and Ederer C 2011 Appl. Phys. Lett. 99 081916
- [69] Holinsworth B S, Mazumdar D, Sims H, Sun Q C, Yurtisigi M K, Sarker S K, Gupta A, Butler W H and Musfeldt J L 2013 Appl. Phys. Lett. 103 082406
- [70] Labchir N, Hannour A, Hssi A A, Vincent D, Abouabassi K, Ihlal A and Sajieddine M 2020 Mater. Sci. Semicond. Process. 111 104992
- [71] Labchir N, Amaterz E, Hannour A, Ait Hssi A, Vincent D, Ihlal A and Sajieddine M 2020 Water Environ. Res. 92 759–65
- [72] Erdem D, Bingham N S, Heiligtag F J, Pilet N, Warnicke P, Heyderman L J and Niederberger M 2016 Adv. Funct. Mater. 26 1954–63
- [73] Ravindra A V, Padhan P and Prellier W 2012 Appl. Phys. Lett. 101 161902
- [74] Jadhav G L, More S D, Kale C M and Jadhav K M 2019 Physica B 555 61–68
- [75] Sharma D and Khare N 2016 AIP Adv. 6 085005

- [76] Kancharla R and Vudayagiri A 2023 J. Supercond. Nov. Magn. 36 119–30
- [77] Jundale V A, Chorage G Y and Yadav A A 2021 Mater. Today 43 2678–81
- [78] Jundale V A and Yadav A A 2022 J. Mater. Sci. Mater. Electron. 33 19612–26
- [79] Dhabekar K and Kant K M 2021 Physica B 603 412752
- [80] Kumar S, Munjal S and Khare N 2017 J. Phys. Chem. Solids 105 86–89
- [81] Ndione P F, Shi Y, Stevanovic V, Lany S, Zakutayev A, Parilla P A, Perkins J D, Berry J J, Ginley D S and Toney M F 2014 Adv. Funct. Mater. 24 610–8
- [82] Wu C, Guo W, Zhen C, Wang H, Li G, Ma L and Hou D 2019 J. Appl. Phys. 126 043901
- [83] Guo W, Zhen C, Wu C, Wu X, Li G and Ma L 2018 Ceram. Int. 44 12539–46
- [84] Zhen C, Zhang X, Wei W, Guo W, Pant A, Xu X, Shen J,
 Ma L and Hou D 2018 J. Phys. D: Appl. Phys. 51 145308
- [85] Sharona H, Loukya B, Bhat U, Sahu R, Vishal B, Silwal P, Gupta A and Datta R 2017 J. Appl. Phys. 122 225301
- [86] Zhang K, Zhen C, Wei W, Guo W, Tang G, Ma L, Hou D and Wu X 2017 *RSC Adv.* **7** 36026–33
- [87] Hu L, Wu L, Liao M, Hu X and Fang X 2012 *Adv. Funct. Mater.* 22 998–1004
- [88] Silwal P, Miao L, Stern I, Zhou X, Hu J and Ho Kim D 2012 Appl. Phys. Lett. 100 032102
- [89] Windisch C F, Ferris K F, Exarhos G J and Sharma S K 2002 Thin Solid Films 420–421 89–99
- [90] Windisch C F, Ferris K F and Exarhos G J 2001 J. Vac. Sci. Technol. A 19 1647–51
- [91] Windisch J, Exarhos G J, Ferris K F, Engelhard M H and Stewart D C 2001 Thin Solid Films 398–399 45–52
- [92] Abbas Q, Siyal S H, Mateen A, Hassan N U, Idrees A, Rehman Z U, Din E M T E, Bajaber M A and Javed M S 2022 Materials 15 4499
- [93] Liu Z, Tan H, Liu D, Liu X, Xin J, Xie J, Zhao M, Song L, Dai L and Liu H 2019 Adv. Sci. 6 1801829
- [94] Wu C, Zhen C, Zhang X, Xu X, Xie J, Ma L, Zhao D and Hou D 2022 J. Phys. Chem. Solids 160 110321
- [95] Wada T, Namiki W, Tsuchiya T, Kan D, Shimakawa Y, Higuchi T and Terabe K 2022 Jpn. J. Appl. Phys. 61 SM1002
- [96] Kim J and Dho J 2023 Thin Solid Films **781** 139978

- [97] Wang M et al 2019 Adv. Mater. 31 1900458
- [98] Kuang M, Zhang Y X, Li T T, Li K F, Zhang S M, Li G and Zhang W 2015 J. Power Sources 283 270–8
- [99] Shi X, Bernasek S L and Selloni A 2017 J. Phys. Chem. C 121 3929–37
- [100] Wei S, Wan C, Zhang L, Liu X, Tian W, Su J, Cheng W and Wu Y 2022 Chem. Eng J. 429 132242
- [101] Silwal P, Miao L, Hu J, Spinu L, Ho Kim D and Talbayev D 2013 J. Appl. Phys. 114 103704
- [102] Han X, Song L, Ding J, Hu L, Xu C and Wang Y 2020 Mater. Lett. 278 128400
- [103] Lovett A J, Daramalla V, Sayed F N, Nayak D, de H-óra M, Grey C P, Dutton S E and MacManus-Driscoll J L 2023 ACS Energy Lett. 8 3437–42
- [104] Wang W, Du Q, Hu Z, Wu J, Wang Z and Liu M 2023 J. Magn. Magn. Mater. 580 170660
- [105] Wu C, Liu L, Xu R, Zhang K, Zhen C, Ma L and Hou D 2021 Mater. Sci. Eng. B 263 114886
- [106] Dileep K, Loukya B, Silwal P, Gupta A and Datta R 2014 J. Phys. D: Appl. Phys. 47 405001
- [107] Dupin J-C, Gonbeau D, Vinatier P and Levasseur A 2000 Phys. Chem. Chem. Phys. 2 1319–24
- [108] Gurlo A, Bârsan N, Oprea A, Sahm M, Sahm T and Weimar U 2004 Appl. Phys. Lett. 85 2280–2
- [109] Gurlo A, Sahm M, Oprea A, Barsan N and Weimar U 2004 Sens. Actuators B 102 291–8
- [110] Demuth J E, Thompson W J, Dinardo N J and Imbihl R 1986 Phys. Rev. Lett. 56 1408–11
- [111] Alonso M, Cimino R and Horn K 1990 *Phys. Rev. Lett.* **64** 1947–50
- [112] Stiles K and Kahn A 1988 Phys. Rev. Lett. 60 440-3
- [113] Arrhenius S 1889 Z. Phys. Chem. 4 226-48
- [114] Chen X, Zhang X, Koten M A, Chen H, Xiao Z, Zhang L, Shield J E, Dowben P A and Hong X 2017 Adv. Mater. 29 1701385
- [115] Vaz C A F, Shin Y J, Bibes M, Rabe K M, Walker F J and Ahn C H 2021 Appl. Phys. Rev. 8 041308
- [116] Zhang Y-S, Chen B-J, Deng X, Guan Z, Chen B-B, Chen Y, Zhong N, Xiang P-H and Duan C-G 2022 J. Mater. Chem. C 10 11654–63
- [117] Nakano M, Shibuya K, Okuyama D, Hatano T, Ono S, Kawasaki M, Iwasa Y and Tokura Y 2012 Nature 487 459–62